





# Angular selection of transmitted light and enhanced spontaneous emission in grating-coupled hyperbolic metamaterials

DASOL LEE,<sup>1,4</sup> MINKYUNG KIM,<sup>1,4</sup>  JONGMIN LEE,<sup>2</sup> BYOUNGSU KO,<sup>1</sup> HUI JOON PARK,<sup>2,5</sup> AND JUNSUK RHO<sup>1,3,6</sup> 

<sup>1</sup>*Department of Mechanical Engineering, Pohang University of Science and Technology (POSTECH), Pohang 37673, Republic of Korea*

<sup>2</sup>*Department of Organic and Nano Engineering, Hanyang University, Seoul 04763, Republic of Korea*

<sup>3</sup>*Department of Chemical Engineering, Pohang University of Science and Technology (POSTECH), Pohang 37673, Republic of Korea*

<sup>4</sup>*These authors contributed equally to this work*

<sup>5</sup>*huijoon@hanyang.ac.kr*

<sup>6</sup>*jsrho@postech.ac.kr*

**Abstract:** We propose dielectric grating-coupled hyperbolic metamaterials as a functional device that shows angular selection of transmitted light and enhanced radiative emission rate. We numerically demonstrate that the surface plasmon polaritons in the hyperbolic metamaterials can be effectively outcoupled to the surrounding space by using gratings and facilitate control of the light transmission in the visible frequency. We confirm that the high density of states and the effect of outcoupled plasmonic modes of the proposed structure lead to the increase of Purcell factor and radiative emission. This work will provide multifunctionalities in sensing and imaging systems that use hyperbolic metamaterials.

© 2021 Optical Society of America under the terms of the [OSA Open Access Publishing Agreement](#)

## 1. Introduction

Hyperbolic metamaterials (HMMs) [1,2] composed of alternating subwavelength layers of metal and dielectric or arrays of nanorods of metal and dielectric have shown numerous applications [3–11]. These HMMs exhibit uniaxial anisotropy with unique optical characteristics due to their hyperbolic dispersion relation characterized by an effective permittivity tensor in which the real parts of the diagonal components have opposite signs. In the hyperbolic region, HMMs support large propagating wavevectors that can be coupled to surface plasmon polaritons (SPPs), which foster various applications such as subwavelength imaging [12–20], focusing [21–29], and spontaneous emission enhancement [30–40].

Enhancement in spontaneous emission is an important property of HMMs for applications to single-photon sources, biosensing, and imaging. HMMs that support large wavevectors result in a huge local density of states (DOS). Various studies of metasurfaces, microcavity, and photonic crystals have shown spontaneous emission increase using the cavity Purcell effect [41–47]. However, those attempts of microcavity and photonic crystals are limited to narrowband spectral operation due to their resonance properties. In contrast, multilayered HMMs typically have hyperbolic dispersion in a broad range of the visible spectrum and thus can substantially broaden the bandwidth of the spontaneous emission enhancement. Introduction of nanopatterns to HMMs further increases the Purcell factor and radiative emission to the far-field by overwhelming the non-radiative properties of plasmonic modes in HMMs [40,48–55].

Nanopatterned structures can also facilitate selective control of SPPs in HMMs or plasmonic structures. The SPPs generated near the HMMs or plasmonic structures under transverse magnetic (TM)-polarized light are evanescent and cannot be transferred to the far-field unless a coupling

mechanism is used. Grating structures can selectively transmit propagating SPPs by diffraction, which can give angular selection in response to the incident angle [56–58].

We present grating-coupled hyperbolic metamaterials (GCHMM) composed of one-dimensional dielectric gratings on multilayered HMM. In general, HMMs that do not have an outcoupling principle can increase emission rate of emitters, but the increase remains localized to the substrate and is impractical. Thus, to use this enhanced emission practically, functional devices must be developed. We numerically demonstrate that the grating structure on HMMs can selectively transmit the SPPs, which can be used to excite emitters. Simultaneously, large DOS from the GCHMM can increase Purcell factor and radiative emission over a broad range of wavelength. The proposed GCHMM will be advantageous in realizing compact and ultra-sensitive imaging and sensing devices that can simplify the optical setup without excitation filters.

## 2. Results and discussion

### 2.1. Design of GCHMM

A GCHMM is composed of four pairs of silver (Ag) and silicon dioxide ( $\text{SiO}_2$ ) coupled with one-dimensional dielectric gratings on a glass substrate (Fig. 1(a)). The layer thicknesses are  $t_m$  ( $t_d$ ) for Ag ( $\text{SiO}_2$ ), and both are set as 10 nm. The filling ratio of Ag is defined as  $f_{ratio} = t_m/(t_m + t_d)$ , thus  $f_{ratio} = 0.5$ ; this choice optimizes angular selective transmittance in the visible region. Dielectric gratings that have period  $p = 500$  nm, width  $w = 250$  nm, and thickness  $t_g = 100$  nm are placed on the HMM. TM-polarized light illuminates the GCHMM with an incident angle of  $\theta$  (Fig. 1(a), inset).

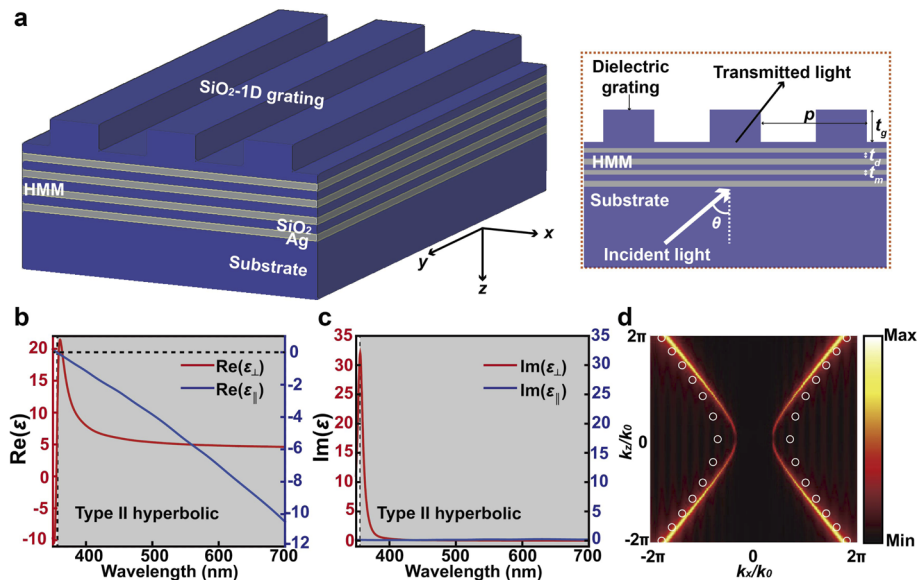


**Fig. 1.** (a) Schematic of a GCHMM. On a multilayer HMM composed of four pairs of silver (Ag) and silicon dioxide ( $\text{SiO}_2$ ), a one-dimensional dielectric grating structure is placed. Both thicknesses of Ag ( $t_m$ ) and  $\text{SiO}_2$  ( $t_d$ ) are 10 nm. Dielectric gratings have period  $p = 500$  nm and thickness  $t_g = 100$  nm. (b) Real and (c) imaginary parts of the effective permittivities along the axis perpendicular and parallel to the anisotropy axis. (d) Theoretical (white dots) and numerically calculated (color map) hyperbolic isofrequency contour at 600 nm.

The effective permittivity tensor of the proposed Ag/SiO<sub>2</sub> HMM multilayer can be calculated using effective media theory as [59]

$$\varepsilon_{eff} = \begin{pmatrix} \varepsilon_{\perp} & 0 & 0 \\ 0 & \varepsilon_{\perp} & 0 \\ 0 & 0 & \varepsilon_{\parallel} \end{pmatrix}, \quad (1)$$

where the subscript  $\perp$  and  $\parallel$  correspond respectively to direction perpendicular and parallel to the anisotropy axis. Each effective permittivity tensor is defined as  $\varepsilon_{\perp} = \frac{\varepsilon_m t_m + \varepsilon_d t_d}{t_m + t_d}$  and  $\varepsilon_{\parallel}^{-1} = \frac{\varepsilon_m^{-1} t_m + \varepsilon_d^{-1} t_d}{t_m + t_d}$ , where  $\varepsilon_m$  and  $\varepsilon_d$  indicate permittivity of Ag and SiO<sub>2</sub>, respectively, which are obtained from the literatures [60,61]. In the whole visible regime,  $\varepsilon_{\perp} > 0$  and  $\varepsilon_{\parallel} < 0$ , so type II hyperbolic dispersion occurs (Figs. 1(b) and 1(c)).

The isofrequency contour (IFC) of the TM mode propagating in the anisotropic medium can be described as [1,2]

$$\frac{k_x^2}{\varepsilon_{\parallel}} + \frac{k_z^2}{\varepsilon_{\perp}} = \frac{\omega^2}{c^2}. \quad (2)$$

Especially when the real parts of the permittivities of the HMMs have opposite sign, IFC shows a hyperbolic shape. The Ag and SiO<sub>2</sub> multilayer supports a hyperbolic dispersion (Fig. 1(d), white dots). In such a medium, a dipole that is oriented along the anisotropic axis generates the following electric field distribution along the anisotropic axis [62],

$$E_z = p_0 k^2 \varepsilon_{\parallel} \sqrt{\varepsilon_{\perp}} \frac{e^{ikr_e}}{r_e^3} \left[ x^2 + y^2 - \left( \frac{1}{ikr_e} + \frac{1}{k^2 r_e^2} \right) (x^2 + y^2 - \frac{2\varepsilon_{\perp}}{\varepsilon_{\parallel}} z^2) \right], \quad (3)$$

where  $r_e = \sqrt{\varepsilon_{\parallel}(x^2 + y^2) + \varepsilon_{\perp} z^2}$ ,  $k$  is the wave number, and  $p_0$  is a dipole moment. A Fourier transformed image of  $E_z$  also agrees well with the hyperbolic IFC (Fig. 1(d), color map).

## 2.2. Angular selection of transmitted light in GCHMM

If the momentum of an angled incidence matches that of SPPs, the incident light excites SPPs. They are localized and decay exponentially away from the surfaces in a planar interface, but become radiative by the coupled dielectric gratings. To investigate the relationship between  $\theta$  and wavelength  $\lambda$ , we perform two-dimensional numerical simulations in the  $x$ - $z$  plane by using the finite-element method (FEM) COMSOL Multiphysics commercial software. We apply Bloch boundary condition along the  $x$ -axis, and add perfectly matched layers along the  $z$ -axis. Diffraction orders of -1, 0, and 1 are included.

Transmittance has spectrally narrow characteristics in which the wavelength  $\lambda_{\max}$  of the highest transmittance depends on  $\theta$  under TM-polarized light (Fig. 2(a)). This angular selection of transmitted light is observed in the whole visible range (Fig. 2(b)). The transmitted spectra at  $\theta = 55^\circ$ ,  $61^\circ$  and  $68^\circ$  have  $\lambda_{\max}$  at red, green, and blue in the visible region, respectively. The spectrum of the transmitted light provides the angular selection to separate the wavelength regime by simple control of  $\theta$  without additional optical components such as a bandpass filter. Strong field enhancement appears only when the momentum of incident light matches the momentum of SPPs (Fig. 2(b), inset). The highly focused field can be observed near HMM surface and coupled with gratings, and becomes radiative light (Fig. 2(b), inset (i)). In contrast, light that is not injected in the resonance angle cannot be coupled and radiative out of HMM (Fig. 2(b), inset (ii)). The kinks in Fig. 2(a) are Rayleigh anomalies that can be observed in grating at the transition between propagating and evanescent modes [63].

For a fixed schematic, the parameters that affect the transmission efficiency are  $t_g$ ,  $t_m$  and  $t_d$  (see Appendix A, Figs. 6–8). To optimize the structure, we defined the figure of merit (FOM) as

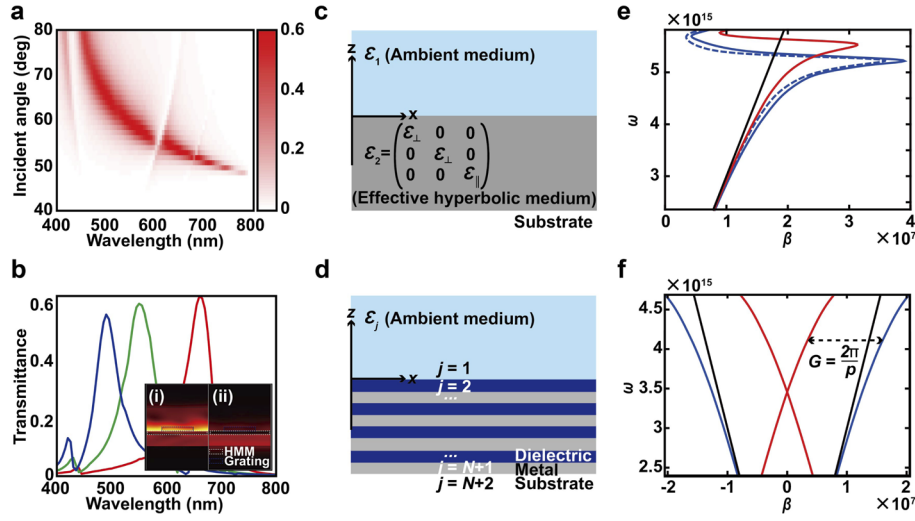


**Fig. 2.** (a) Color map of transmittance according to wavelength and incident angle. (b) Selected spectra at specific incident angles of  $55^\circ$  (red),  $61^\circ$  (green) and  $68^\circ$  (blue); insets: electric field distributions in cross-sectional plane at  $\lambda = 610$  nm with  $\theta$  (i) at resonance angle, and (ii) off resonance angle. (c, d) Schematic of ambient and hyperbolic medium assuming the multilayer as (c) an effective hyperbolic medium or (d) a realistic multilayer structure as it is. (e) Dispersion relations of SPPs between air and the HMM obtained by the effective medium approximation (blue dashed) and exact method (blue solid). Dispersion of SPPs between air and Ag is shown as a reference (red line). (f) Dispersion of SPPs without dielectric gratings (blue curve) and with dielectric gratings (red curve) that lead to momentum matching. Light lines are indicated as black.

the highest transmittance at the wavelengths of 488 and 532 nm. The FOMs are calculated by normalizing the transmittance of a given structure by transmittance at  $t_g = 100$  nm and  $t_m = t_d = 10$  nm (see Appendix B, Fig. 9). The result shows that the current structure has the highest FOM, which directly leads to strong outcoupling efficiency with SPPs in HMM.

To understand how the large wavevector component is delivered to the far-field, we examine SPPs at the interface of a HMM and air while excluding gratings. The dispersion relation of SPPs can be obtained by either assuming the multilayer as an effective hyperbolic medium (Fig. 2(c)) or by directly calculating coupled modes of SPPs in each interface (Fig. 2(d)). Firstly, propagation constant  $\beta$  of SPPs between air ( $\epsilon_{\text{air}} = 1$ ) and the effective HMM can be obtained by generalizing analytical calculation of SPPs at an interface of two isotropic media [64] to that of an isotropic and anisotropic media (Fig. 2(c)). Without loss of generality, we can set the  $x$ -axis as the propagation direction of SPP. Then the electric field can be expressed as  $E(x, y, z) = E(z)e^{i\beta x}$ . Under the non-magnetic assumption ( $\mu_r = 1$ ), the electromagnetic fields of TM modes at each medium satisfy

$$\begin{aligned} \frac{\partial E_x}{\partial z} - i\beta E_z &= i\omega\mu_0 H_y, \\ \frac{\partial H_y}{\partial z} &= i\omega\epsilon_0\epsilon_x E_x, \\ i\beta H_y &= -i\omega\epsilon_0\epsilon_z E_z, \end{aligned} \quad (4)$$

where  $\epsilon_0$  is the permittivity of free space. The wave equation in terms of magnetic field is

$$\frac{1}{\epsilon_x} \frac{\partial^2 H_y}{\partial z^2} + (k_0^2 - \frac{1}{\epsilon_z} \beta^2) H_y = 0, \quad (5)$$

where  $k_0$  is the free space wave number. Electromagnetic fields at each side of medium can be expressed as

$$\begin{aligned} H_{1y} &= A_1 e^{i\beta x} e^{-k_1 z}, \\ E_{1x} &= \frac{iA_1 k_1}{\omega \varepsilon_0 \varepsilon_1} e^{i\beta x} e^{-k_1 z}, \\ E_{1z} &= -\frac{A_1 \beta}{\omega \varepsilon_0 \varepsilon_1} e^{i\beta x} e^{-k_1 z}, \end{aligned} \quad (6)$$

and

$$\begin{aligned} H_{2y} &= A_2 e^{i\beta x} e^{k_2 z}, \\ E_{2x} &= -\frac{iA_2 k_2}{\omega \varepsilon_0 \varepsilon_{\perp}} e^{i\beta x} e^{k_2 z}, \\ E_{2z} &= -\frac{A_2 \beta}{\omega \varepsilon_0 \varepsilon_{\parallel}} e^{i\beta x} e^{k_2 z}, \end{aligned} \quad (7)$$

where the numeric subscripts specify the medium (1 for air and 2 for HMM). Substituting Eq. (6) and Eq. (7) to Eq. (5) yields

$$\begin{aligned} k_1^2 &= \beta^2 - k_0^2 \varepsilon_1, \\ k_2^2 &= \frac{\varepsilon_{\perp}}{\varepsilon_{\parallel}} \beta^2 - k_0^2 \varepsilon_{\perp}. \end{aligned} \quad (8)$$

Imposing boundary conditions (continuity of  $H_y$ ,  $D_x$  and  $D_z$ ) and substitution of the results to Eq. (8) gives the dispersion relation of SPPs as

$$\beta = k_0 \sqrt{\frac{\varepsilon_1 - \varepsilon_1^2 / \varepsilon_{\perp}}{1 - \varepsilon_1^2 / \varepsilon_{\perp} \varepsilon_{\parallel}}}. \quad (9)$$

When  $\varepsilon_2$  is a scalar ( $\varepsilon_{\parallel} = \varepsilon_{\perp} = \varepsilon_2$ ), the dispersion reduces to  $\beta = k_0 \sqrt{\varepsilon_1 \varepsilon_2 / (\varepsilon_1 + \varepsilon_2)}$  which is consistent with the well-known dispersion of SPPs between two isotropic media that have opposite signs of permittivity [64].

Coupled modes of SPPs of multilayer structures embedded by air and substrate can be calculated numerically without effective medium approximation. In a microscopic view, each interface between Ag and SiO<sub>2</sub> supports SPPs. The thickness of each layer is much smaller than the wavelength regime, so the decay lengths of SPPs are larger than the thickness of each layer, and collective coupling of SPPs occurs. Here, we show derivation of dispersion of coupled SPPs. Electromagnetic field components of the TM modes in  $j$ -th medium ( $j \in \{1, 2, \dots, N+2\}$  where  $N$  is the total number of layers, (Fig. 2(d))) can be described as

$$\begin{aligned} H_y^j &= C_j e^{i\beta x} e^{k_j z} + D_j e^{i\beta x} e^{-k_j z}, \\ E_x^j &= -iC_j \frac{k_j}{\omega \varepsilon_0 \varepsilon_j} e^{i\beta x} e^{k_j z} + iD_j \frac{k_j}{\omega \varepsilon_0 \varepsilon_j} e^{i\beta x} e^{-k_j z}, \\ E_z^j &= -C_j \frac{\beta}{\omega \varepsilon_0 \varepsilon_j} e^{i\beta x} e^{k_j z} - D_j \frac{\beta}{\omega \varepsilon_0 \varepsilon_j} e^{i\beta x} e^{-k_j z}, \end{aligned} \quad (10)$$

where  $\varepsilon_j$  is the permittivity of  $j$ -th medium and  $k_j = \sqrt{\beta^2 - k_0^2 \varepsilon_j}$  is the imaginary part of the  $z$ -component of the wavevector in the  $j$ -th medium. Fields at the ambient medium and the substrate should decay, so  $C_1 = D_{N+2} = 0$ . Also, the field amplitude of the substrate can be set as unity ( $C_{N+2} = 1$ ). The dispersion relation of the coupled SPPs can be calculated numerically

by solving sequential boundary conditions. The relationship between field amplitudes of  $j$ -th and  $(j + 1)$ -th medium ( $j = 1, 2, \dots, N + 1$ ) can be described as

$$L_j \begin{pmatrix} C_j \\ D_j \end{pmatrix} = M_j \begin{pmatrix} C_{j+1} \\ D_{j+1} \end{pmatrix},$$

$$L_j = \begin{pmatrix} e^{k_j z_j} & e^{-k_j z_j} \\ -\frac{k_j}{\varepsilon_j} e^{k_j z_j} & \frac{k_j}{\varepsilon_j} e^{-k_j z_j} \end{pmatrix}, \quad (11)$$

$$M_j = \begin{pmatrix} e^{k_{j+1} z_j} & e^{-k_{j+1} z_j} \\ -\frac{k_{j+1}}{\varepsilon_{j+1}} e^{k_{j+1} z_j} & \frac{k_{j+1}}{\varepsilon_{j+1}} e^{-k_{j+1} z_j} \end{pmatrix},$$

where  $z_j$  is the  $z$ -coordinate of interface between  $j$ -th and  $(j + 1)$ -th medium. Then, field amplitudes of the ambient medium and substrate are related as

$$\begin{pmatrix} C_1 \\ D_1 \end{pmatrix} = L_1^{-1} M_1 L_2^{-1} M_2 \cdots L_{N+1}^{-1} M_{N+1} \begin{pmatrix} C_{N+2} \\ D_{N+2} \end{pmatrix} = \prod_{j=1}^{N+1} L_j^{-1} M_j \begin{pmatrix} C_{N+2} \\ D_{N+2} \end{pmatrix}. \quad (12)$$

Now we have two equations and two unknown variables  $\beta$  and  $D_1$ . Therefore, the dispersion relation of the coupled SPPs is numerically solvable. Dispersion relations of SPPs between air and the HMM composed of four pairs of Ag and SiO<sub>2</sub> with 10 nm thickness are calculated by two methods (Fig. 2(e), blue curves). SPPs between air and the HMM have higher propagation constant compared to the dispersion of SPPs between air and Ag (Fig. 2(e), red curve).

SPPs have wavevector higher than that of light cone in whole visible frequency (Fig. 2(f), blue curves), and this momentum mismatch hinders coupling of SPPs. However, the gratings compensate for the phase mismatch by adding momentum along the  $x$ -axis for TM mode as

$$k_0 \sin \theta_t + mG = \beta, \quad (13)$$

where  $\theta_t$  is a transmitted angle,  $m$  is a grating order, and  $G = \frac{2\pi}{p}$  is the reciprocal vector of the gratings. Now, dispersion of SPPs with  $m = \pm 1$  falls within the light cone (Fig. 2(f), red curves). The calculated diffraction efficiency proves that only the first-order light can be radiative. Thus, adjusting  $\theta$  of TM-polarized incidence enables angular selective transmission that has a specific bandwidth in the entire visible regime with transmittance  $\sim 0.6$ . Without gratings, light with the incident angle does not transmit HMM, but mostly reflects. The zero transmission of the zero-th diffraction is attributed to the absence of a real solution of  $\theta$  that satisfies the phase matching.

### 2.3. Spontaneous emission enhancement on GCHMM

The angular selection of the transmitted light can be applied to excite emitters on the GCHMM. Various commercial fluorescent beads or quantum dots can be selectively excited without excitation filters, so this method is applicable to fluorescent imaging or sensing systems, in which the emission of emitters is largely enhanced by the GCHMM (see Appendix D, Fig. 11). The high wavevector component of the HMM opens a new emission channel, leading to increase in the spontaneous emission rate. The HMM has type II hyperbolic dispersion in the whole visible range (Figs. 1(b) and 1(c)), so the increased emission can be observed in a broad visible regime. To examine how HMM alters the dipole emission, Purcell factor and radiative enhancement (RE)

are considered as [40]

$$\text{Purcell factor} = \frac{P_{\text{total}}}{P_{0,\text{total}}}, \quad (14)$$

$$\text{RE} = \frac{P_{\text{rad}}}{P_{0,\text{total}}}, \quad (15)$$

where  $P_{0,\text{total}} = \mu_0 \omega^2 p_0^2 / 12\pi c$  is the total power emitted by the dipole in free space where  $\mu_0$  is the permeability of free space,  $\omega$  is angular frequency, and  $c$  is speed of light.  $P_{\text{total}}$  is the total power and  $P_{\text{rad}}$  is the radiative power emitted by the dipole. Purcell factor quantifies increase in the total emitted power from a dipole, and therefore includes dipole power that is absorbed due to ohmic losses. Such non-radiative power cannot reach a detector in the far-field and thus is not useful for applications. RE is a ratio of the radiative power of a dipole to the total emitted power of a dipole in free space, and therefore evaluates enhancement in radiative power.

We perform a numerical simulation to investigate the behaviors of emitters near the GCHMM. We use three-dimensional simulations to calculate Purcell factors near a bare substrate, a HMM multilayer, and a GCHMM. In each simulation, we set a point dipole source on a corresponding substrate in a domain that has size of  $5\lambda \times 5\lambda \times 5\lambda$ , and applied perfectly-matched layers to all boundaries. We calculate  $P_{\text{total}}$  by integrating all powers at boundaries of a small ( $5 \text{ nm} \times 5 \text{ nm} \times 5 \text{ nm}$ ) box that encloses the dipole source, then use Eq. (14) to obtain the Purcell factor of a dipole placed above 10 nm from the surfaces with polarizations along the  $x$ -,  $y$ -, and  $z$ -directions. We place a dipole at a distance of 10 nm above the surfaces and center between the gratings. Compared to the glass substrate as a reference (Fig. 3(a)), a HMM multilayer (Fig. 3(b)) and a GCHMM (Fig. 3(c)) both clearly show broadband Purcell enhancement of the same order. Despite the anisotropic geometry of the 1D gratings, the Purcell factors of the  $x$ - and  $y$ -polarized dipoles are barely distinguishable (Fig. 3(c)). It is because the dipole is placed closely to the multilayer and the radiative emission characteristic of a dipole is affected largely to its closest environment. A difference between the Purcell factors of the  $x$  and  $y$  polarizations is shown in a 2D spatial map in Appendix E (Fig. 12).

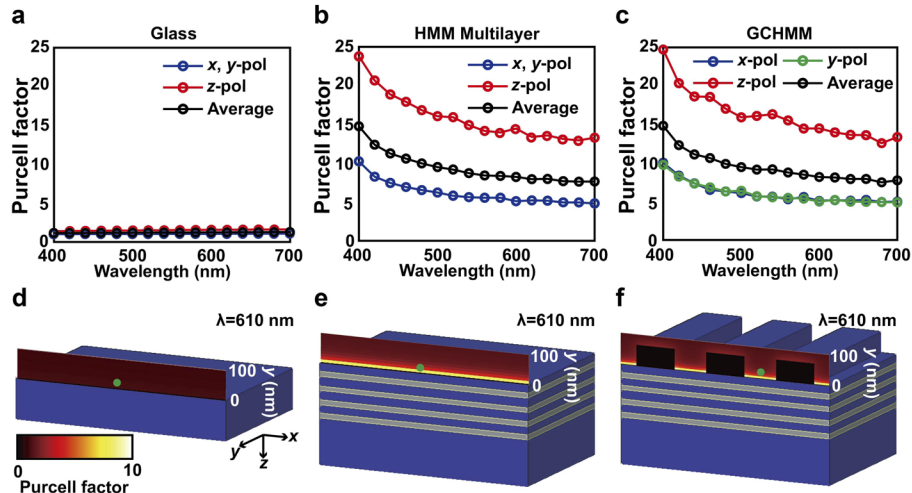


**Fig. 3.** Simulation results of Purcell factor. (a)-(c) Purcell factors above 10 nm from (a) bare glass, (b) HMM multilayer, and (c) GCHMM. (d)-(f) Cross-sectional color maps of Purcell factor on (d) bare glass, (e) HMM multilayer, and (f) GCHMM at the wavelength of 610 nm. A GCHMM shows similar trend of Purcell factor as in the uniform HMM multilayer but much higher than on a bare glass substrate.

We also calculate cross-sectional mappings at  $\lambda = 610$  nm of Purcell factor for dipole emitters placed at different surfaces (Figs. 3(d)–3(f)). The Purcell factor decays exponentially with increasing distance from the multilayer along the  $z$ -axis (Fig. 3(e)). Even a GCHMM follows the trend along the  $z$ -axis, and this trend leads to small differences in the Purcell factor in the  $x$ - $y$  plane due to the gratings (Fig. 3(f)). The GCHMM shows a similar increase in Purcell factor in the  $x$ - $y$  plane from the gratings. However, near gratings that have weak Purcell factor, a different trend occurs because of the distance between emitter and HMMs.

The coupled gratings lead to the outcoupling effect, so the radiative property of emitters is better on the GCHMM than on the bare glass and HMM multilayer (Figs. 4(a)–4(c)). In the GCHMM case, RE of a dipole at central position between periodic gratings is considered. RE is simulated similarly to the Purcell factor except that  $P_{\text{rad}}$  is obtained by integrating powers in a box that contains all of the structures. The size of the box is  $0.9 \times 0.9 \times 0.9$  of the whole domain size excluding the perfectly matched layers. RE of a dipole on a bare glass substrate has the same order as Purcell factor (Fig. 4(a)). This result is attributed to negligible optical losses of glass in the visible range. In contrast, RE near a HMM multilayer or a GCHMM have lower values than Purcell factors, as a result of the high ohmic losses of the multilayers, but the trends are similar (Figs. 4(b) and 4(c)). In particular, RE at short  $\lambda \sim 400$  nm is strongly suppressed by the large imaginary parts of the effective permittivity (Fig. 1(c)). Still, the RE is much higher than that on a bare glass. A difference between the RE of the  $x$  and  $y$  polarizations can be found in Appendix E (Fig. 12).

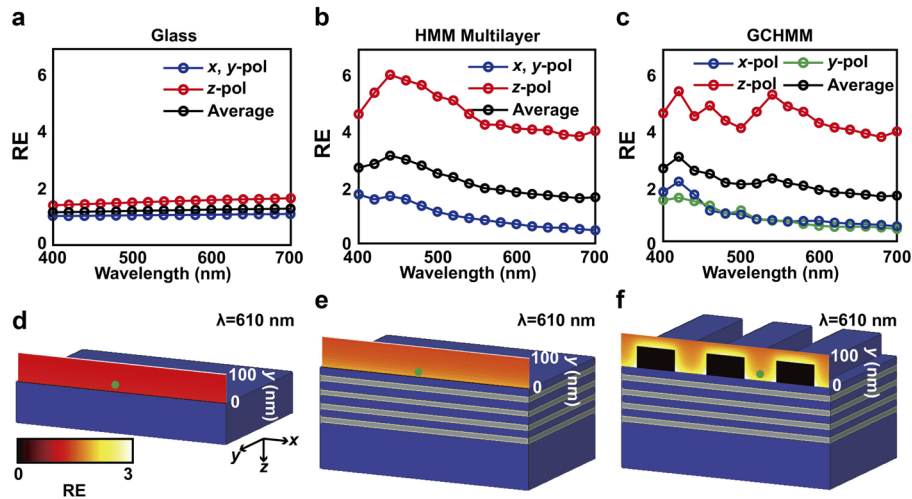


**Fig. 4.** Simulation results of RE. (a)–(c) RE above 10 nm from (a) bare glass, (b) HMM multilayer, and (c) GCHMM. (d)–(f) Cross-sectional color maps of RE on (d) bare glass, (e) HMM multilayer, and (f) GCHMM at the wavelength of 610 nm. The GCHMM shows higher RE along the HMM and gratings surface compared to HMM without gratings.

We also simulate cross-sectional mapping of the RE at  $\lambda = 610$  nm for dipole emitters placed at different surfaces (Figs. 4(d)–4(f)). While spatial variation of RE on the bare glass substrate and HMMs are not significant, the GCHMM achieves strong RE along the surfaces of the gratings and HMM due to their high DOS from the outcoupling effect. The RE is large over a wider spatial range in a GCHMM than in planar multilayers; this trait is suitable for sensing and imaging applications that use emitters. The simulated cross-sectional maps of the Purcell factor and RE at  $\lambda = 532$  nm are described in Appendix C (Fig. 10).

For further investigation of Purcell factor and RE on the GCHMM, we simulate the Purcell factor and RE along the  $z$ -axis at  $x$ -axis positions of 0, 80, 100 nm (Fig. 5(a)) at  $\lambda = 610$  nm. The



Purcell factor decays exponentially with increase in distance from the surface along the  $z$ -axis, regardless of the position of the  $x$ -axis (Fig. 5(b)). Similarly, the simulated RE value decreases as the distance between the dipole and surface increases (Fig. 5(c)), but the decrease is less drastic than in Purcell factor; this attribute is most noticeable near the gratings where the coupling effect exists.

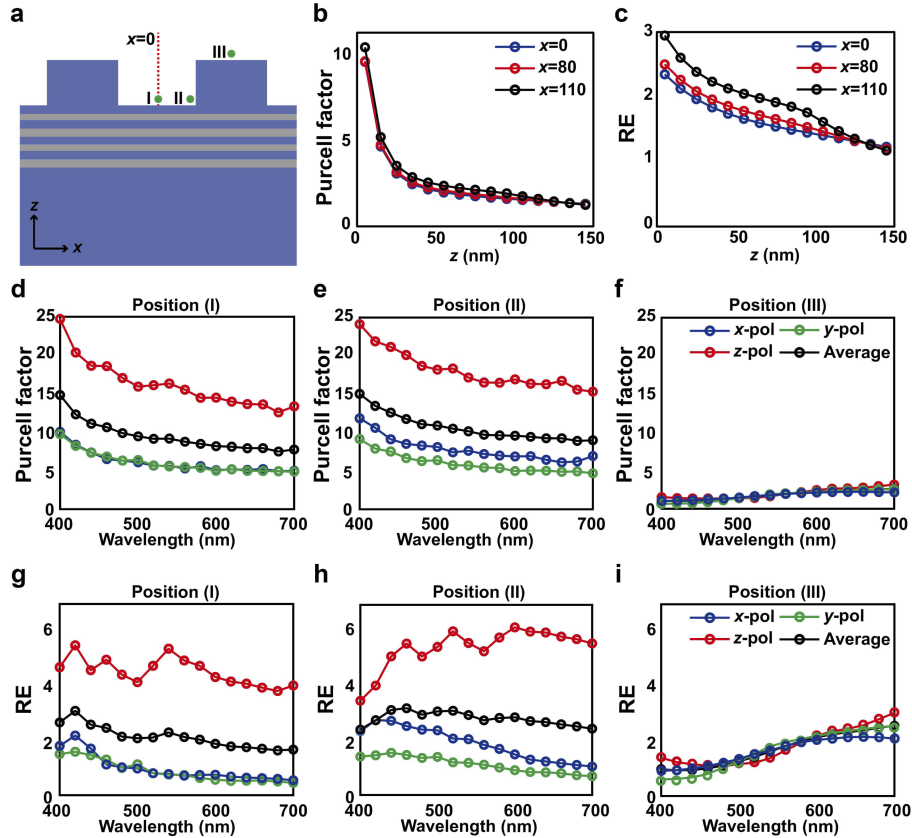


**Fig. 5.** (a) Schematic to mark the positions of dipoles. Simulated (b) Purcell factor and (c) RE at the different  $x$ -axis positions of 0, 80, 110 nm at  $\lambda = 610$  nm. Simulated (d)–(f) Purcell factors and (g)–(i) RE above the 10 nm from surface at positions I–III, respectively.

We also examine Purcell and RE spectra at three different positions (Fig. 5(a), I, II, III) at the center position between gratings, next to the gratings, and on the gratings 10 nm from the surface. The Purcell factor of dipoles at positions of I and II do not differ from each other at each polarization (Figs. 5(d)–5(f)), but the factor is very small at position III. The Purcell factor of a dipole at position II is slightly increased for  $x$ -polarized dipoles due to the adjacent effect with the gratings, but it is low for all polarizations due to the influence of the distance from the HMM in the upper part of the gratings.

The trends in RE (Figs. 5(g)–5(i)) at the same positions resembled those of Purcell factor. The GCHMM supports enhanced RE compared to the HMMs that do not have gratings. Especially, higher RE can be observed close to the gratings within broad range of wavelength region. Due to the coupling effect with gratings, even the surface above the gratings has higher RE than the uniform HMM; this trait may help to increase the external quantum efficiency of emitters. Notably, the coupling using gratings can selectively determine the wavelength range of the transmitted light, and the emitter on the GCHMM can be effectively excited by selecting the appropriate

incident angle. Optimization of the geometry of the nanopatterns may further increase Purcell factor and RE, and yield applications in sensing and imaging that use fluorescence.

### 3. Conclusion

We have numerically demonstrated a GCHMM that simultaneously shows angular selection of transmitted light and enhanced radiative spontaneous emission in the visible region. By using one-dimensional diffraction gratings to outcouple the SPPs in the HMM, the light transmission range can be controlled by selecting the incident angle. A high transmittance near 0.6 is achieved in the visible region; this property is appropriate for use to selectively excite emitters. Numerical simulation results show that emitters on the GCHMM increase Purcell factor and radiative emission due to the high DOS of the GCHMM and the effect of outcoupling of plasmonic modes by gratings. We believe that engineering the DOS of HMMs exploiting the outcoupling principle will find wide applications in fluorescence imaging and sensing, spectroscopy, and light-emitting devices.

### Appendix A: parametric studies on transmittance spectra of GCHMM

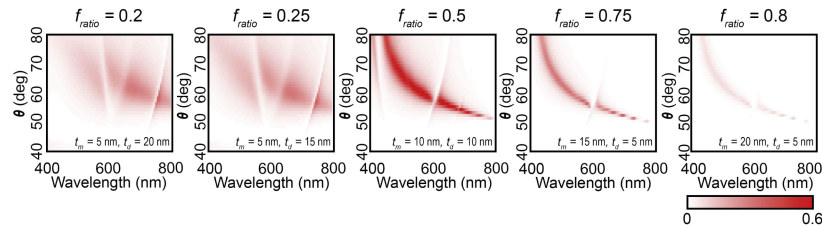


**Fig. 6.** Color map of transmittance according to wavelength and incident angle  $\theta$  with various filling ratio ( $f_{ratio}$ ).  $t_m$  and  $t_d$  are the thickness of metal and dielectric layer, respectively.

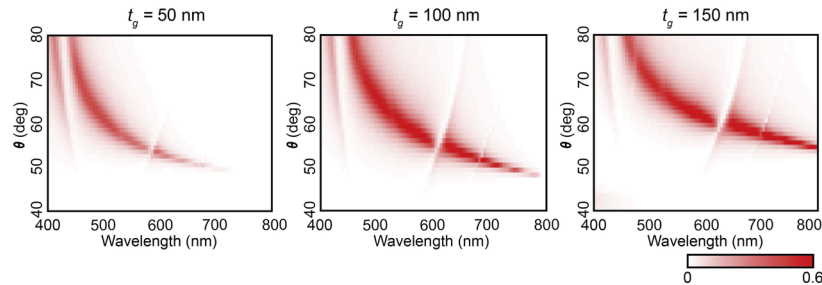


**Fig. 7.** Color map of transmittance according to wavelength and  $\theta$  with different thickness of gratings ( $t_g$ ).

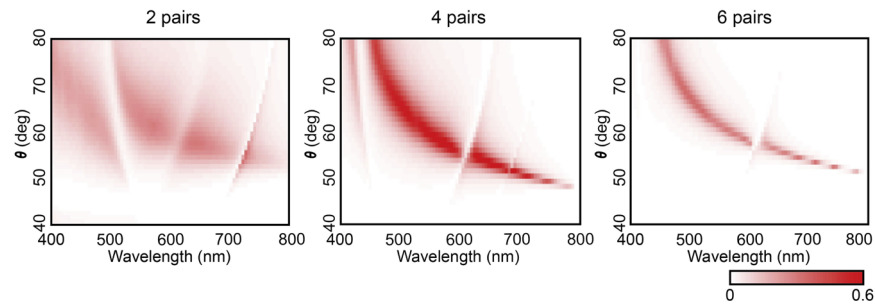


**Fig. 8.** Color map of transmittance according to wavelength and  $\theta$  with the different number of metal-dielectric layers.

### Appendix B: the figure of merit to optimize the parameters of GCHMM

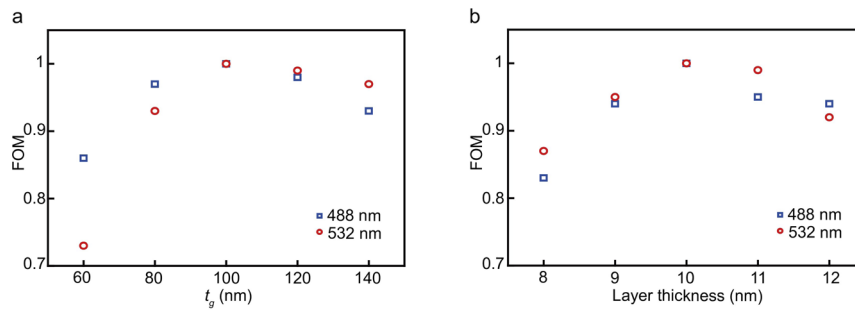


**Fig. 9.** The figure of merit (FOM) calculated by normalizing the transmittance of a given structure by transmittance at  $t_g = 100$  nm and  $t_m = t_d = 10$  nm. (a) FOM according to different  $t_g$  when  $t_m = t_d$  are fixed to 10 nm. (b) FOM according to different layer thickness when  $t_g$  are fixed to 100 nm.

### Appendix C: simulated Purcell factor and RE at $\lambda = 532$ nm

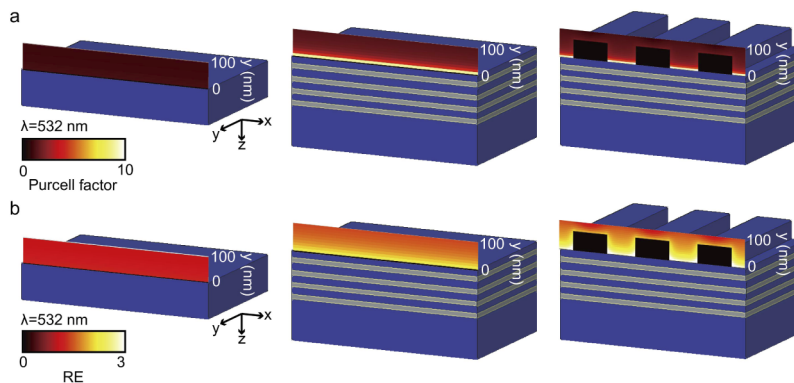


**Fig. 10.** Simulation results of (a) Purcell factor and (b) radiative enhancement (RE) at  $\lambda = 532$  nm above 10 nm from bare glass, HMM multilayer, and GCHMM.

## Appendix D: feasible application scheme for imaging and sensing

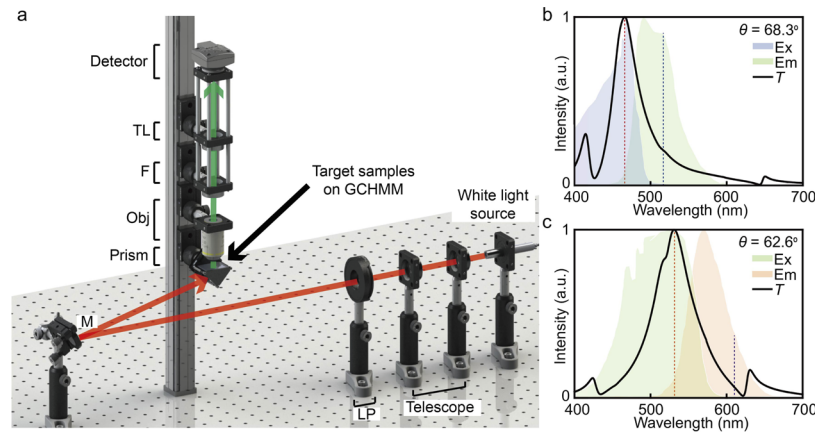


**Fig. 11.** (a) Feasible optical setup for imaging and sensing that use GCHMM with index matching medium. Target fluorescent sample can be placed on GCHMM. Desired wavelength of light can be selectively illuminated to target samples by adjusting  $\theta$ , and the emitted signal from emitters can be captured to the detector. Here, LP: linear polarizer, M: Mirror, Obj: objective lens, F: emission filter, TL: Tube lens. (b)-(c) Practical applications using commercial fluorescent dyes. Here, we select and focus on two specific  $\theta$  that fit the excitation wavelengths of emitters. (b) An example of use with commercial yellow-green fluorescent dye (Polysciences, Inc., 17156-2). The excitation (Ex), emission (Em) wavelengths and selected transmittance ( $T$ ) by  $\theta$  are represented as blue-, green-colored region and black line, respectively. The coincidence of maximum excitation peak near 490 nm (dashed red line) and resonance of transmitted light become target for efficient excitation condition. At the angle of  $68.3^\circ$ , the maximum of transmitted light is at 488 nm which can expect high emission from fluorescence dye. (c) Another example of red fluorescent dye (Polysciences, Inc., 19111-2). The excitation, emission wavelengths and selected transmittance are represented as green-, red-colored region and black line, respectively. At the angle of  $62.6^\circ$ , the resonance of transmitted light is coincided to the maximum excitation wavelength of the fluorescence beads near 532 nm. The dashed blue lines in each graph [Figs. 11(b) and 11(c)] represent the emission peaks (532 nm and 610 nm) which are used in the manuscript for simulation.

## Appendix E: differences in Purcell factors and RE of $x$ and $y$ polarizations

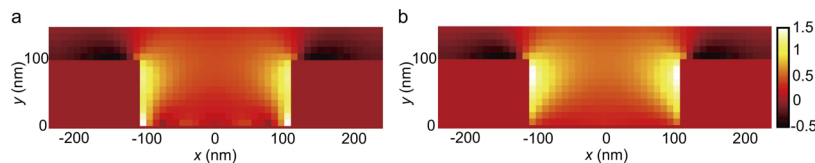


**Fig. 12.** 2D spatial maps of (a) a difference between the Purcell factors of the  $x$  and  $y$  polarizations and (b) a difference between the RE of the  $x$  and  $y$  polarizations.

**Funding.** Samsung (IO201215-08187-01); National Research Foundation of Korea (CAMP-2019M3A6B3030637, NRF-2019R1A2C3003129, NRF-2019R1A5A8080290).

**Acknowledgments.** D. L. acknowledges the PIURI fellowship funded by POSTECH. M. K. acknowledges the Global Ph.D. fellowship (NRF-2017H1A2A1043204) funded by the Ministry of Education of the Korean government.

**Disclosures.** The authors declare no conflicts of interest.

**Data availability.** Data underlying the results presented in this paper are not publicly available at this time but may be obtained from the authors upon reasonable request.

## References

1. A. Poddubny, I. Iorsh, P. Belov, and Y. Kivshar, "Hyperbolic metamaterials," *Nat. Photonics* **7**(12), 948–957 (2013).
2. L. Ferrari, C. Wu, D. Lepage, X. Zhang, and Z. Liu, "Hyperbolic metamaterials and their applications," *Prog. Quantum Electron.* **40**, 1–40 (2015).
3. Y.-C. Chang, C.-H. Liu, C.-H. Liu, S. Zhang, S. R. Marder, E. E. Narimanov, Z. Zhong, and T. B. Norris, "Realization of mid-infrared graphene hyperbolic metamaterials," *Nat. Commun.* **7**(1), 10568 (2016).
4. J. Yao, Z. Liu, Y. Liu, Y. Wang, C. Sun, G. Bartal, A. M. Stacy, and X. Zhang, "Optical negative refraction in bulk metamaterials of nanowires," *Science* **321**(5891), 930 (2008).
5. Y. Liu, G. Bartal, and X. Zhang, "All-angle negative refraction and imaging in a bulk medium made of metallic nanowires in the visible region," *Opt. Express* **16**(20), 15439–15448 (2008).
6. Y. Liu and X. Zhang, "Metasurfaces for manipulating surface plasmons," *Appl. Phys. Lett.* **103**(14), 141101 (2013).
7. A. A. High, R. C. Devlin, A. Dibos, M. Polking, D. S. Wild, J. Perczel, N. P. De Leon, M. D. Lukin, and H. Park, "Visible-frequency hyperbolic metasurface," *Nature* **522**(7555), 192–196 (2015).
8. S. Bang, S. So, and J. Rho, "Realization of broadband negative refraction in visible range using vertically stacked hyperbolic metamaterials," *Sci. Rep.* **9**(1), 14093 (2019).
9. M. Kim, D. Lee, T. H. Kim, Y. Yang, H. J. Park, and J. Rho, "Observation of enhanced optical spin hall effect in a vertical hyperbolic metamaterial," *ACS Photonics* **6**(10), 2530–2536 (2019).
10. H. Cho, S. So, T. Badloe, S. Bang, and J. Rho, "Critical layer thickness analysis of vertically stacked hyperbolic metamaterials for effective negative refraction generation," *Adv. Theory Simul.* **3**, 2000138 (2020).
11. M. Kim, D. Lee, H. Cho, B. Min, and J. Rho, "Spin hall effect of light with near-unity efficiency in the microwave," *Laser Photonics Rev.* **15**, 2000393 (2021).
12. Z. Jacob, L. V. Alekseyev, and E. Narimanov, "Optical hyperlens: far-field imaging beyond the diffraction limit," *Opt. Express* **14**(18), 8247–8256 (2006).
13. Z. Liu, H. Lee, Y. Xiong, C. Sun, and X. Zhang, "Far-field optical hyperlens magnifying sub-diffraction-limited objects," *Science* **315**(5819), 1686 (2007).
14. J. Rho, Z. Ye, Y. Xiong, X. Yin, Z. Liu, H. Choi, G. Bartal, and X. Zhang, "Spherical hyperlens for two-dimensional sub-diffractional imaging at visible frequencies," *Nat. Commun.* **1**(1), 143 (2010).
15. D. Lu and Z. Liu, "Hyperlenses and metalenses for far-field super-resolution imaging," *Nat. Commun.* **3**(1), 1205 (2012).
16. J. Sun, M. I. Shalaev, and N. M. Litchinitser, "Experimental demonstration of a non-resonant hyperlens in the visible spectral range," *Nat. Commun.* **6**(1), 7201 (2015).
17. D. Lee, Y. D. Kim, M. Kim, S. So, H.-J. Choi, J. Mun, D. M. Nguyen, T. Badloe, J. G. Ok, K. Kim, H. Lee, and J. Rho, "Realization of wafer-scale hyperlens device for sub-diffractional biomolecular imaging," *ACS Photonics* **5**(7), 2549–2554 (2018).
18. M. Byun, D. Lee, M. Kim, Y. Kim, K. Kim, J. G. Ok, J. Rho, and H. Lee, "Demonstration of nanoimprinted hyperlens array for high-throughput sub-diffraction imaging," *Sci. Rep.* **7**(1), 1–11 (2017).
19. D. Lee, M. Kim, S. So, I. Kim, G. Yoon, K. Kim, and J. Rho, "Demonstration of a hyperlens-integrated microscope and super-resolution imaging," *J. Vis. Exp.* **127**, e55968 (2017).
20. S. So and J. Rho, "Geometrically flat hyperlens designed by transformation optics," *J. Phys. D: Appl. Phys.* **52**(19), 194003 (2019).
21. T. Xu, Y. Zhao, J. Ma, C. Wang, J. Cui, C. Du, and X. Luo, "Sub-diffraction-limited interference photolithography with metamaterials," *Opt. Express* **16**(18), 13579–13584 (2008).
22. M. Kim, S. So, K. Yao, Y. Liu, and J. Rho, "Deep sub-wavelength nanofocusing of uv-visible light by hyperbolic metamaterials," *Sci. Rep.* **6**(1), 38645 (2016).
23. S. Ishii, A. V. Kildishev, E. Narimanov, V. M. Shalaev, and V. P. Drachev, "Sub-wavelength interference pattern from volume plasmon polaritons in a hyperbolic medium," *Laser Photonics Rev.* **7**(2), 265–271 (2013).
24. G. Liang, C. Wang, Z. Zhao, Y. Wang, N. Yao, P. Gao, Y. Luo, G. Gao, Q. Zhao, and X. Luo, "Squeezing bulk plasmon polaritons through hyperbolic metamaterials for large area deep subwavelength interference lithography," *Adv. Opt. Mater.* **3**, 1248–1256 (2015).
25. G. Li, J. Li, and K. W. Cheah, "Subwavelength focusing using a hyperbolic medium with a single slit," *Appl. Opt.* **50**(31), G27–G30 (2011).
26. S. Dai, Q. Ma, T. Andersen, A. Mcleod, Z. Fei, M. Liu, M. Wagner, K. Watanabe, T. Taniguchi, M. Thiemens, F. Keilmann, P. Jarillo-Herrero, M. M. Fogler, and D. N. Basov, "Subdiffractional focusing and guiding of polaritonic rays in a natural hyperbolic material," *Nat. Commun.* **6**(1), 6963 (2015).
27. J. Sun, T. Xu, and N. M. Litchinitser, "Experimental demonstration of demagnifying hyperlens," *Nano Lett.* **16**(12), 7905–7909 (2016).
28. L. Liu, P. Gao, K. Liu, W. Kong, Z. Zhao, M. Pu, C. Wang, and X. Luo, "Nanofocusing of circularly polarized bessell-type plasmon polaritons with hyperbolic metamaterials," *Mater. Horiz.* **4**(2), 290–296 (2017).

29. X. Chen, C. Zhang, F. Yang, G. Liang, Q. Li, and L. J. Guo, "Plasmonic lithography utilizing epsilon near zero hyperbolic metamaterial," *ACS Nano* **11**(10), 9863–9868 (2017).
30. W. D. Newman, C. L. Cortes, and Z. Jacob, "Enhanced and directional single-photon emission in hyperbolic metamaterials," *J. Opt. Soc. Am. B* **30**(4), 766–775 (2013).
31. T. Galfsky, H. Krishnamoorthy, W. Newman, E. Narimanov, Z. Jacob, and V. Menon, "Active hyperbolic metamaterials: enhanced spontaneous emission and light extraction," *Optica* **2**(1), 62–65 (2015).
32. M. Noginov, H. Li, Y. A. Barnakov, D. Dryden, G. Nataraj, G. Zhu, C. Bonner, M. Mayy, Z. Jacob, and E. Narimanov, "Controlling spontaneous emission with metamaterials," *Opt. Lett.* **35**(11), 1863–1865 (2010).
33. H. N. Krishnamoorthy, Z. Jacob, E. Narimanov, I. Kretzschmar, and V. M. Menon, "Topological transitions in metamaterials," *Science* **336**(6078), 205–209 (2012).
34. J. K. Kitur, L. Gu, T. Tumulur, C. Bonner, and M. A. Noginov, "Stimulated emission of surface plasmons on top of metamaterials with hyperbolic dispersion," *ACS Photonics* **2**(8), 1019–1024 (2015).
35. L. Ferrari, J. S. T. Smalley, Y. Fainman, and Z. Liu, "Hyperbolic metamaterials for dispersion-assisted directional light emission," *Nanoscale* **9**(26), 9034–9048 (2017).
36. P. Ginzburg, D. J. Roth, M. E. Nasir, P. Segovia, A. V. Krasavin, J. Levitt, L. M. Hirvonen, B. Wells, K. Suhling, D. Richards, V. A. Podolskiy, and A. V. Zayats, "Spontaneous emission in non-local materials," *Light: Sci. Appl.* **6**(6), e16273 (2017).
37. H.-I. Lin, K.-C. Shen, Y.-M. Liao, Y.-H. Li, P. Perumal, G. Haider, B. H. Cheng, W.-C. Liao, S.-Y. Lin, W.-J. Lin, T.-Y. Lin, and Y.-F. Chen, "Integration of nanoscale light emitters and hyperbolic metamaterials: an efficient platform for the enhancement of random laser action," *ACS Photonics* **5**(3), 718–727 (2018).
38. K. J. Lee, Y. U. Lee, S. J. Kim, and P. André, "Hyperbolic dispersion dominant regime identified through spontaneous emission variations near metamaterial interfaces," *Adv. Mater. Interfaces* **5**, 1701629 (2018).
39. Y. Shen, Y. Yan, A. N. Brigeman, H. Kim, and N. C. Giebink, "Efficient upper-excited state fluorescence in an organic hyperbolic metamaterial," *Nano Lett.* **18**(3), 1693–1698 (2018).
40. D. Lu, J. J. Kan, E. E. Fullerton, and Z. Liu, "Enhancing spontaneous emission rates of molecules using nanopatterned multilayer hyperbolic metamaterials," *Nat. Nanotechnol.* **9**(1), 48–53 (2014).
41. C. Tserkezis, R. Esteban, D. O. Sigle, J. Mertens, L. O. Herrmann, J. J. Baumberg, and J. Aizpurua, "Hybridization of plasmonic antenna and cavity modes: Extreme optics of nanoparticle-on-mirror nanogaps," *Phys. Rev. A* **92**(5), 053811 (2015).
42. T. B. Hoang, G. M. Akselrod, C. Argyropoulos, J. Huang, D. R. Smith, and M. H. Mikkelsen, "Ultrafast spontaneous emission source using plasmonic nanoantennas," *Nat. Commun.* **6**(1), 7788 (2015).
43. S. C. Indukuri, J. Bar-David, N. Mazurski, and U. Levy, "Ultrascale mode volume hyperbolic nanocavities for enhanced light-matter interaction at the nanoscale," *ACS Nano* **13**(10), 11770–11780 (2019).
44. J. Yao, X. Yang, X. Yin, G. Bartal, and X. Zhang, "Three-dimensional nanometer-scale optical cavities of indefinite medium," *Proc. Natl. Acad. Sci. U. S. A.* **108**(28), 11327–11331 (2011).
45. X. Yang, J. Yao, J. Rho, X. Yin, and X. Zhang, "Experimental realization of three-dimensional indefinite cavities at the nanoscale with anomalous scaling laws," *Nat. Photonics* **6**(7), 450–454 (2012).
46. Z. Wang, K. Yao, M. Chen, H. Chen, and Y. Liu, "Manipulating smith-purcell emission with babinet metasurfaces," *Phys. Rev. Lett.* **117**(15), 157401 (2016).
47. L. Li, K. Yao, Z. Wang, and Y. Liu, "Harnessing evanescent waves by bianisotropic metasurfaces," *Laser Photonics Rev.* **14**, 1900244 (2020).
48. L. Ferrari, D. Lu, D. Lepage, and Z. Liu, "Enhanced spontaneous emission inside hyperbolic metamaterials," *Opt. Express* **22**(4), 4301–4306 (2014).
49. L. Wang, S. Li, B. Zhang, Y. Qin, Z. Tian, Y. Fang, Y. Li, Z. Liu, and Y. Mei, "Asymmetrically curved hyperbolic metamaterial structure with gradient thicknesses for enhanced directional spontaneous emission," *ACS Appl. Mater. Interfaces* **10**(9), 7704–7708 (2018).
50. A. Kala, F. A. Inam, S.-A. Biehs, P. Vaity, and V. G. Achanta, "Hyperbolic metamaterial with quantum dots for enhanced emission and collection efficiencies," *Adv. Opt. Mater.* **8**, 2000368 (2020).
51. L. Li, W. Wang, T. S. Luk, X. Yang, and J. Gao, "Enhanced quantum dot spontaneous emission with multilayer metamaterial nanostructures," *ACS Photonics* **4**(3), 501–508 (2017).
52. K. V. Sreekanth, K. H. Krishna, A. De Luca, and G. Strangi, "Large spontaneous emission rate enhancement in grating coupled hyperbolic metamaterials," *Sci. Rep.* **4**(1), 6340 (2015).
53. D. Lu, H. Qian, K. Wang, H. Shen, F. Wei, Y. Jiang, E. E. Fullerton, P. K. Yu, and Z. Liu, "Nanostructuring multilayer hyperbolic metamaterials for ultrafast and bright green inorganic quantum wells," *Adv. Mater.* **30**, 1706411 (2018).
54. K. H. Krishna, K. Sreekanth, and G. Strangi, "Dye-embedded and nanopatterned hyperbolic metamaterials for spontaneous emission rate enhancement," *J. Opt. Soc. Am. B* **33**(6), 1038–1043 (2016).
55. J. Kim, V. P. Drachev, Z. Jacob, G. V. Naik, A. Boltasseva, E. E. Narimanov, and V. M. Shalaev, "Improving the radiative decay rate for dye molecules with hyperbolic metamaterials," *Opt. Express* **20**(7), 8100–8116 (2012).
56. J. M. Choi, K. Eom, S. Hwang, Y. Lee, S. B. Jun, K. M. Byun, and S. J. Kim, "Multi-color fluorescence imaging based on plasmonic wavelength selection and double illumination by white light," *Opt. Express* **22**(5), 5977–5985 (2014).
57. K. M. Byun, S. J. Kim, and D. Kim, "Grating-coupled transmission-type surface plasmon resonance sensors based on dielectric and metallic gratings," *Appl. Opt.* **46**(23), 5703–5708 (2007).

58. S. H. Choi, S. J. Kim, and K. M. Byun, "Design study for transmission improvement of resonant surface plasmons using dielectric diffraction gratings," *Appl. Opt.* **48**(15), 2924–2931 (2009).
59. A. N. Poddubny, P. A. Belov, and Y. S. Kivshar, "Spontaneous radiation of a finite-size dipole emitter in hyperbolic media," *Phys. Rev. A* **84**(2), 023807 (2011).
60. P. B. Johnson and R.-W. Christy, "Optical constants of the noble metals," *Phys. Rev. B* **6**(12), 4370–4379 (1972).
61. I. H. Malitson, "Interspecimen comparison of the refractive index of fused silica," *J. Opt. Soc. Am.* **55**(10), 1205–1209 (1965).
62. A. S. Potemkin, A. N. Poddubny, P. A. Belov, and Y. S. Kivshar, "Green function for hyperbolic media," *Phys. Rev. A* **86**(2), 023848 (2012).
63. J. W. Strutt, "On the dynamical theory of gratings," *Proc. R. Soc. A* **79**(532), 399–416 (1907).
64. S. A. Maier, *Plasmonics: fundamentals and applications* (Springer Science & Business Media, 2007).